Technology

Molecular Cell

Visualizing the Path of DNA through Proteins Using DREEM Imaging

Graphical Abstract

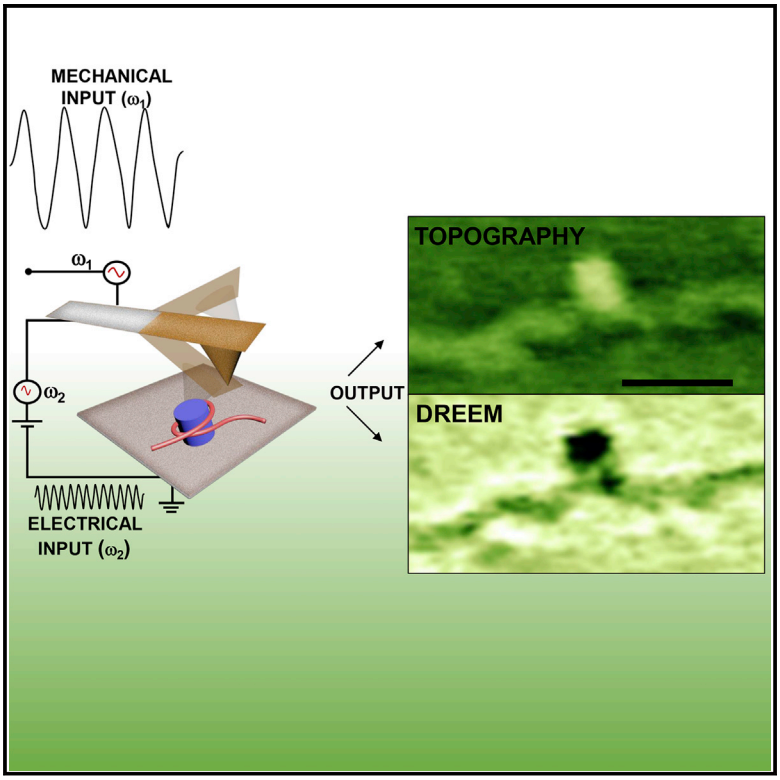

Authors

Dong Wu, Parminder Kaur, Zimeng M. Li, Kira C. Bradford, Hong Wang, Dorothy A. Erie

Correspondence

hong_wang@ncsu.edu (H.W.), derie@unc.edu (D.A.E.)

In Brief

Wu et al. developed a dual resonance frequency imaging method that simultaneously captures atomic force microscopy topographic and electrostatic force gradient images. This method reveals DNA wrapping around histones and the path of DNA as it passes through both single-protein and multiprotein mismatch repair complexes.

Highlights

- Dual-frequency atomic and electrostatic force microscopy of protein-DNA complexes
- Imaging the topographic and electrostatic features of protein-DNA complexes
- Visualizing DNA in nucleosomes and mismatch repair complexes via their electrostatics

Wu et al., 2016, Molecular Cell *61*, 315–323
January 21, 2016
http://dx.doi.org/10.1016/j.molcel.2015.12.012

CellPress

Molecular Cell
Technology

Visualizing the Path of DNA through Proteins Using DREEM Imaging

Dong Wu,[1,6] Parminder Kaur,[2,6] Zimeng M. Li,[3] Kira C. Bradford,[1] Hong Wang,[2,4,*] and Dorothy A. Erie[1,5,*]
[1]Department of Chemistry, University of North Carolina, Chapel Hill, NC 27599, USA
[2]Department of Physics, North Carolina State University, Raleigh, NC 27695, USA
[3]Department of Physics and Astronomy, University of North Carolina, Chapel Hill, NC 27599, USA
[4]Center for Human Health and the Environment, North Carolina State University, Raleigh, NC 27695, USA
[5]Curriculum in Applied Sciences and Engineering, University of North Carolina, Chapel Hill, NC 27599, USA
[6]Co-first author
*Correspondence: hong_wang@ncsu.edu (H.W.), derie@unc.edu (D.A.E.)
http://dx.doi.org/10.1016/j.molcel.2015.12.012

SUMMARY

Many cellular functions require the assembly of multiprotein-DNA complexes. A growing area of structural biology aims to characterize these dynamic structures by combining atomic-resolution crystal structures with lower-resolution data from techniques that provide distributions of species, such as small-angle X-ray scattering, electron microscopy, and atomic force microscopy (AFM). A significant limitation in these combinatorial methods is localization of the DNA within the multiprotein complex. Here, we combine AFM with an electrostatic force microscopy (EFM) method to develop an exquisitely sensitive dual-resonance-frequency-enhanced EFM (DREEM) capable of resolving DNA within protein-DNA complexes. Imaging of nucleosomes and DNA mismatch repair complexes demonstrates that DREEM can reveal both the path of the DNA wrapping around histones and the path of DNA as it passes through both single proteins and multiprotein complexes. Finally, DREEM imaging requires only minor modifications of many existing commercial AFMs, making the technique readily available.

INTRODUCTION

DNA transactions in the cell, such as replication, repair, and transcription, require the assembly of multiple proteins on DNA. Determining the structures of these complexes is essential to understanding their function; however, several factors make characterization of multiprotein-DNA complexes particularly difficult. First, many of the individual proteins are large and contain structured domains connected to one another by intrinsically disordered regions, making them conformationally diverse. Second, the assembly of the different proteins is not necessarily an ordered process, which results in a heterogeneous population of complexes with different conformations and containing different protein stoichiometries (Luijsterburg et al., 2010). Finally, the assembly process may occur over long DNA lengths and/or bring distal DNA regions together. An emerging area of structural biology, which is beginning to address this problem, is the combination of high-resolution data from crystallography and NMR with lower-resolution data from techniques such as small-angle X-ray scattering, which provides estimates of the distribution of conformational states (Hennig and Sattler, 2014; Hura et al., 2013a, 2013b; Williams et al., 2014), and electron microscopy (EM) and atomic force microscopy (AFM), which provide images of individual complexes (Bustamante et al., 1994; Erie et al., 1994; Griffith, 2013; Griffith and Christiansen, 1978; Janićijević et al., 2003; Lohr et al., 2007; Lyubchenko et al., 2001; Maletta et al., 2014; Moreno-Herrero et al., 2005; Sanchez et al., 2013; Trinh et al., 2012; Villarreal and Stewart, 2014; Wanner and Schroeder-Reiter, 2008; Yang et al., 2003; Yeh et al., 2012). Although these hybrid methods are promising, a significant limitation to the existing lower-resolution techniques is their limited capability for resolving the location of the nucleic acids within protein-DNA complexes. Phosphorus mapping through electron spectroscopic imaging (ESI) has been used to characterize the nucleic acid distribution in transcriptionally active chromatin (Bazett-Jones et al., 1996). In addition, recent advances in the sorting of particles in cryoEM datasets are beginning to allow visualization of multiple conformations (Orlova and Saibil, 2010), and the trajectories of DNA have been estimated by tagging the end of DNA with streptavidin (Miyata et al., 2005; Villarreal and Stewart, 2014). Finally, recent EM studies revealed the location of the DNA in human RNA polymerase complexes (He et al., 2013) and the RNA in the ribosome (e.g., Brown et al., 2014; Fernández et al., 2013). Currently, no microscopy method allows visualization of DNA within flexible and/or large heterogeneous protein-DNA complexes. Because scanning force microscopy methods can provide images of individual complexes and because both proteins and DNA are significantly charged and interactions between proteins and DNA result in charge neutralization, we reasoned that it may be possible to visualize the path of DNA within individual protein-DNA complexes by high-resolution imaging of their electrostatic properties.

Electrostatic force microscopy (EFM) and Kelvin probe force microscopy (KPFM) have been used to image the

electrostatic surface potential of a large variety of materials with high spatial resolution and sensitivity (Barth et al., 2011; Melitz et al., 2011). There are several different modes of EFM and KPFM. In many applications, a modulated bias voltage ($V_{DC} + V_{AC}sin(\omega t)$) is applied between the tip and sample. This bias generates an attractive electrostatic force between the tip and the sample, $F_{el} = -(1/2)(\partial C/\partial z)\Delta V^2$, where $\Delta V = (V_{DC} - \Delta\phi_{TS}) + V_{AC}\sin(\omega t)$, which is expressed as the sum of three spectral components (Glatzel, 2003; Melitz et al., 2011; Nonnenmacher et al., 1991):

$$F_{DC} = -\frac{1}{2}\frac{\partial C}{\partial z}\left[(\Delta\phi_{TS} - V_{DC})^2 + \frac{V_{AC}^2}{2}\right] \quad \text{(Equation 1)}$$

$$F_{\omega} = \frac{\partial C}{\partial z}\left[(\Delta\phi_{TS} - V_{DC})V_{AC}\sin(\omega t)\right] \quad \text{(Equation 2)}$$

$$F_{2\omega} = \frac{1}{4}\frac{\partial C}{\partial z}V_{AC}^2\cos(2\omega t) \quad \text{(Equation 3)}$$

where $\Delta\phi_{TS}$ and $\partial C/\partial z$ are the contact potential difference and capacitance gradient, respectively, between the tip and the sample, and z is normal to the surface. This force is used to induce a vibration in the cantilever at the frequency of the AC bias (ω). In KPFM, a feedback loop is used to adjust V_{DC} such that it compensates for $\Delta\phi_{TS}$, thereby nullifying F_{ω} and generating a potential map of the surface; whereas, in EFM, there is no feedback voltage, and although EFM does not measure surface potential, images of the electrostatic properties of the surface are produced by monitoring the amplitude and/or phase of the induced vibration. Dual-frequency single-pass techniques, where the topography and the surface electrical potential are monitored simultaneously have the highest sensitivity (Barth et al., 2011; Glatzel, 2003; Leung et al., 2010; Thompson et al., 2013). In fact, dual-frequency KPFM has been used to obtain images of DNA (Leung et al., 2010) and transcription complexes (Mikamo-Satoh et al., 2009); however, no details about the DNA in the transcription complexes were revealed.

Considering the weak electrostatic signals generated by DNA and proteins, we developed a sensitive high-resolution dual-resonance-frequency-enhanced EFM (DREEM) to resolve the DNA within protein-DNA complexes deposited on mica (Figure 1). This dual frequency technique enables simultaneous collection of AFM topographic and DREEM images. DREEM images reveal DNA wrapping around individual nucleosomes and the path of DNA passing through DNA mismatch repair (MMR) proteins. These data yield unprecedented details about DNA conformations within individual protein-DNA complexes.

DESIGN

We adapted and extended the dual-frequency single-pass techniques that take advantage of the resonance properties of the cantilever (Glatzel, 2003; Kikukawa et al., 1996; Leung et al., 2010; Stark et al., 2007; Thompson et al., 2013; Ziegler et al., 2007). To simultaneously obtain topographic and DREEM images, we mechanically vibrate the cantilever near the fundamental resonance (ω_1), as is done in standard repulsive intermittent contact mode topographic imaging, while applying a static and a modulated bias voltage (V_{DC} and V_{AC}, respectively) to the tip at the first overtone (ω_2) to monitor the surface electrical properties (Figure 1) (Stark et al., 2007). Instead of using the DC bias to nullify F_{ω} as is done in KPFM, we use an AC bias at ω_2 to generate a vibration at ω_2 and apply the DC bias after engaging in repulsive mode to optimize the amplitude at ω_2 for electrostatic imaging. We then monitor the vibration amplitude (A_{ω_2}) and phase (φ_{ω_2}) as a function of sample position. Because there is no feedback at the first overtone, the DREEM amplitude and phase signals depend on both the strength of the electrostatic force and force gradient, including the static force gradient (F'_{DC}) (Supplemental Information) (Cleveland et al., 1998; Rodríguez and García, 2004; Tamayo, 2005; Thompson et al., 2013). In addition, other forces may contribute to the signal at ω_2 if they are not canceled by the feedback at the fundamental frequency (Cleveland et al., 1998; Martínez and García, 2006; Martínez et al., 2008; Rodríguez and García, 2004; Tamayo, 2005; Thompson et al., 2013). Generally, the phase image produces higher contrast due to the nonlinear dependence of the phase on the force gradient and energy dissipation (φ_{ω_2} depends on the arcsine of the force gradient and the energy dissipation) (Cleveland et al., 1998; Rodríguez and García, 2004; Tamayo, 2005). For example, studies using dual-frequency AFM (with mechanically driven vibration at both frequencies) to image antibodies found that the signal to noise ratio for the phase signal is ~50 times higher than that of the amplitude signal at ω_2 (Martínez et al., 2008). Because the force gradient depends on both the capacitance and the electrostatic potential of the sample, changes in either of these properties will contribute to the observed signals. To maximize resolution in both the AFM topographic and DREEM images, we use highly doped sharp silicon cantilevers and operate in repulsive intermittent contact mode. Operating in repulsive mode keeps the tip at a constant minimal distance from the sample, which in turn maximizes the sensitivity of detection of the electrostatic force gradient. Although highly doped silicon cantilevers are the only available cantilevers that are sufficiently sharp to provide high-resolution images, the variability of the oxidation layers on the silicon cantilevers limits the possibilities for quantitative comparison of DREEM signals collected using different cantilevers (see Limitations).

Using the first overtone for electrostatic imaging and the fundamental frequency for topographic imaging has several advantages. First, it is preferable to conduct topographic imaging of soft samples with a minimal force to avoid damage, and the effective force constant at ω_1 (~80 kHz) is approximately 40 times less than that at ω_2 (~500 kHz) [$k_2 = k_1(\omega_2/\omega_1)^2$] (Kokavecz and Mechler, 2008). Second, ω_2 is more sensitive to changes in force gradient than ω_1 because the minimal detectable force gradient is inversely proportional to the frequency and the Q-factor of the resonance peak, which is higher at ω_2 ($Q(\omega_2)$ ~500) than at ω_1 ($Q(\omega_1)$ ~170) (Hoummady and Farnault, 1998). Third, the contribution of the electrostatic interaction between the cantilever and the sample to the electrostatic force is minimized at ω_2, thereby enhancing spatial resolution in the DREEM image (Ding et al., 2009). Fourth, higher eigenmodes provide enhanced phase contrast compared to the fundamental mode of tip

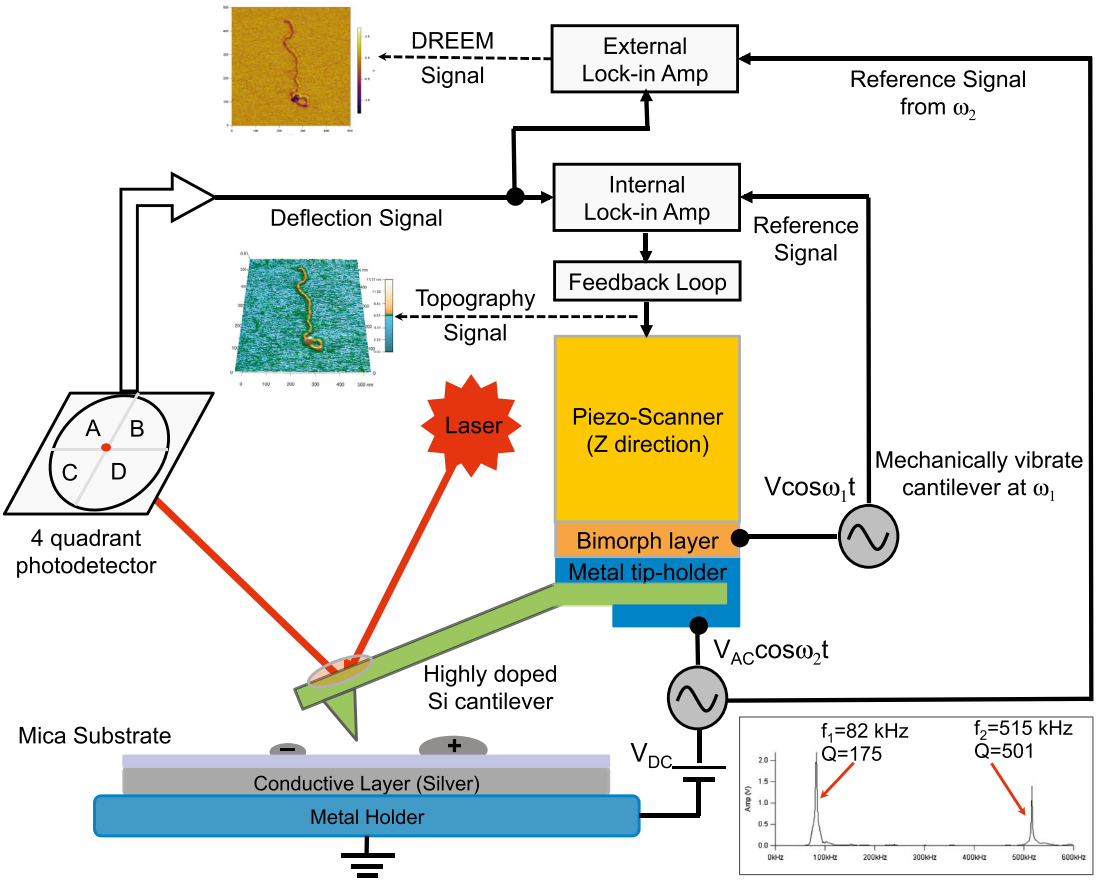

Figure 1. Instrumental Design for Simultaneous AFM and DREEM Imaging

The AFM (MFP-3D, Asylum Research) is operated in repulsive oscillating (intermittent contact) mode with the cantilever mechanically vibrated near its resonance frequency ($\omega_1 = 2\pi f_1$) ($f_1 = \sim$80 kHz for the cantilever used in this study) to collect the topographic information. To simultaneously collect the DREEM image, AC and DC biases are applied to a highly doped silicon cantilever (Nanosensors, PPP-FMR, force constant ~2.8 N/m), with the frequency of the AC bias centered on cantilever's first overtone ($\omega_2 = 2\pi f_2$) ($f_2 \sim$500 kHz). An external lock-in amplifier is used to separate the ω_2 component from the output signal and compare it with the reference input AC signal to generate the electrostatic amplitude and phase signals. The DC bias is maintained constant and is used to adjust the electrical vibration amplitude to produce optimal contrast in the DREEM images. In the current setup, the AC and DC biases can be adjusted from 0 V to 20 V and −2.5 V to 2.5 V, respectively. The inset shows the thermal motion of a typical cantilever used in our experiments as a function of the frequency. The frequencies and Q factors for the fundamental (f_1, Q_1) and first overtone (f_2, Q_2) frequencies are shown by each peak.

oscillation for both AFM and EFM imaging (Martínez et al., 2008; Stark et al., 1999; Thompson et al., 2013).

To determine the optimum voltage for obtaining the highest-resolution DREEM amplitude and phase images, we hold the AC bias constant (usually V_{AC} = 10–20 V) and vary the DC bias between +2.5 V and −2.5 V. The optimum DC bias depends on the tip because the tips can have different extents of oxidation on their surfaces, which affects $\Delta\phi_{TS}$ (Rezek, 2005). Operating in repulsive mode using a cantilever with force constant of ~2.8 N/m, the amplitude of vibration at ω_2 (A_{ω_2}) is ~1 nm, which is 30–50 times smaller than the mechanical vibration amplitude (A_{ω_1}) at the fundamental frequency. This A_{ω_2} is sufficiently large to produce high-quality DREEM images and yet small enough compared to A_{ω_1} that no crosstalk from the DREEM to topographic signals is observed (see below). A_{ω_2} depends not only on the force at ω_2, but also on the force gradient, $\partial F/\partial z$ (*i.e.*, F'), because F' changes the effective spring constant of the cantilever and shifts its resonance frequency, which in turn changes A_{ω_2} (Albrecht et al., 1991). Upon engaging in repulsive mode, the force gradient due to repulsive atomic interactions (F'_a) causes the resonance peak to shift to a higher frequency, significantly reducing A_{ω_2}. In our experiments, A_{ω_2} decreased by approximately a factor of two upon repulsive engage. During scanning, F'_a and F_a are kept constant via feedback on the topographic signal at ω_1, and therefore, changes in $A_{\omega_2}[\Delta A_{\omega_2}(x,y)]$ depend primarily on the electrostatic force and force gradient. For small changes in electrostatic potential and/or capacitance, the frequency shift due to changes in force gradient will dominate $\Delta A_{\omega_2}(x,y)$, with the electrostatic force making only a small contribution (Supplemental Information) (Martin et al., 1987). Notably, monitoring F' instead of F significantly increases spatial resolution and sensitivity, because F' has a shorter distance dependence compared to F (Colchero et al., 2001; Giessibl, 1995; Lei et al., 2004; Martin et al., 1987).

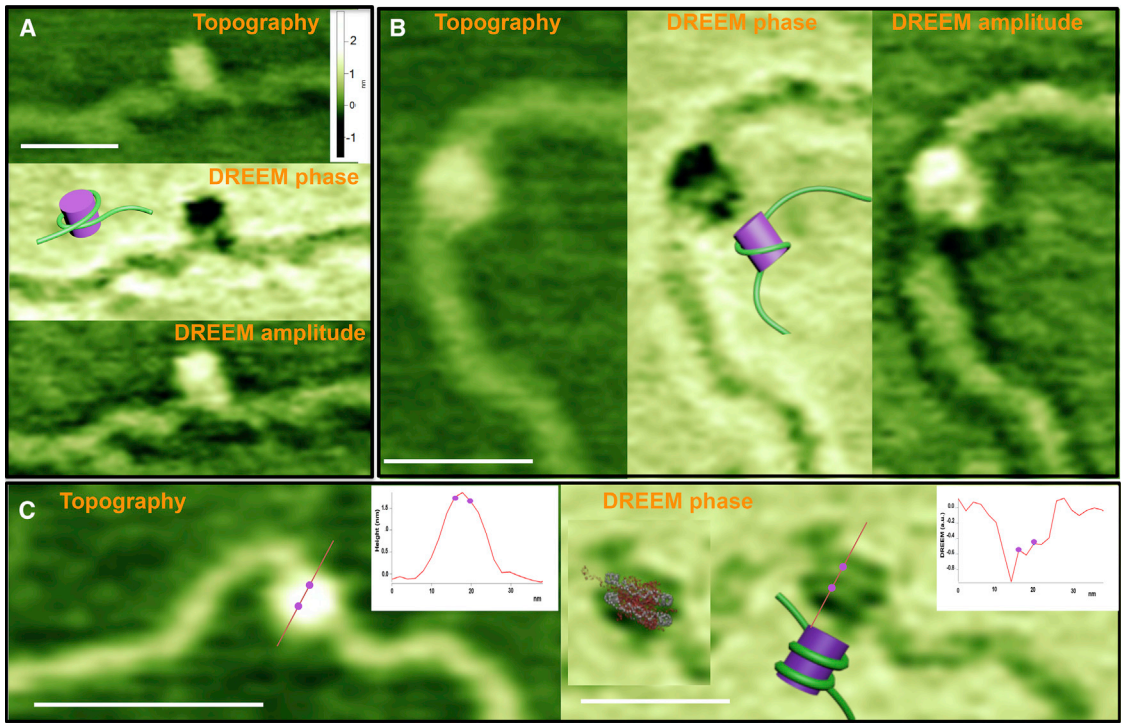

Figure 2. Representative Topographic AFM and DREEM Images of Nucleosomes

(A and B) Topographic (A top, B left), DREEM-phase (A middle, B center), and DREEM amplitude (A bottom, B right) images of nucleosomes showing one DNA wrapping around histones one time.

(C) Topographic (left) and DREEM-phase (right) images of a nucleosome showing DNA wrapping around nucleosomes twice. Insets show graphs of the height cross-section for the line drawn across the nucleosome in topographic (left) and DREEM-phase (right) images. The two dots on the graph correspond to the positions of the two dots shown on the line across the image, which mark the position of the peaks corresponding to the DNA in the DREEM image. The distance between the two peaks corresponding to the two DNA double strands (dots on graph) is 3.4 nm, which is similar to that seen in the crystal structure (~3 nm) (Luger et al., 1997). Cartoon models of the DNA wrapping around histones are shown on each DREEM-phase image (models are not to scale). The crystal structure of a nucleosome (Luger et al., 1997) overlaid on the DREEM-phase image is shown in the inset of the phase image in (C). The white scale bars are 50 nm. All topographic images are scaled to the same height, and the height scale bar is shown in (A). Both the topographic and DREEM-phase images in (C) are sharper than those in (A) and (B) as a result of a sharper AFM tip. All features in the images are seen in both the trace and retrace scans (Figure S2B). Nucleosomes were reconstituted on a 2,743 bp linear fragment containing 147 bp 601 nucleosome positioning sequence. Unlike the images of nucleosomes, DREEM images of free histones show only smooth "hemispherical shape," similar to the topographic images (Figure S2A). See also Figure S2.

RESULTS AND DISCUSSION

We verified the capabilities of DREEM for detecting surface electrical potential by imaging a $BaTiO_3$ thin film, which can maintain a stable polarization state after being polarized by external electrical field (Choi et al., 2004; Gruverman et al., 2009; Trithaveesak et al., 2005). We generated a pattern of very weak negatively and positively charged areas (~2 electrons/nm^2) on a $BaTiO_3$ film (Figure S1A) (Bonnell and Kalinin, 2001) and then imaged the sample with AFM and DREEM with different DC and AC biases (e.g., Figure S1). The topographic image reveals only a rough surface with a large contaminant particle, with no evidence of the charge pattern. In contrast, both the DREEM-phase and amplitude signals clearly show the charge pattern, which corresponds accurately to the differently charged areas (Figure S1B), but show no evidence of the contaminant particle seen in the topographic image. These results demonstrate the capability of DREEM for detecting weak surface charges (<2 electrons/nm^2), with no significant crosstalk between the topographic and DREEM signals. Furthermore, the observation that the contaminant particle does not produce any signal in either the DREEM-phase or amplitude images suggests that the dominant force acting at ω_2 is the electrostatic force.

Visualizing the Path of DNA within Protein-DNA Complexes

To demonstrate the power of DREEM for imaging protein-DNA complexes, we imaged nucleosomes and DNA MMR proteins bound to DNA, as well as free proteins. In the crystal structure of a nucleosomal core particle, 147 base pairs of DNA wrap around the histone octamer 1.67 times (Luger et al., 1997, 2012), whereas in MMR complexes, the DNA passes through DNA mismatch recognition protein MutS (Lamers et al., 2000; Obmolova et al., 2000; Warren et al., 2007), and multiple MutS and MutL proteins can assemble onto DNA containing a mismatch (Elez et al., 2012; Grilley et al., 1989; Hombauer et al., 2011; Kunkel and Erie, 2005; Schofield et al., 2001). The DREEM images of free histones, free MMR proteins, and

DNA show a decrease in the phase and an increase in amplitude, relative to the mica surface, with proteins producing greater contrast than DNA (Figures 2, S2, and S3A), as seen in previous EFM studies (Leung et al., 2010; Mikamo-Satoh et al., 2009). The features seen in the DREEM images of free protein mimic those seen in the topographic images (Figures S2A and S3A).

Figure 2 shows AFM topographic and DREEM images of nucleosomes. In the topographic images, the nucleosomes appear as smooth peaks protruding above the DNA, consistent with previous work (Bustamante et al., 1997; Lohr et al., 2007; Lyubchenko, 2014; Swygert et al., 2014; Wang et al., 2002; Yang et al., 1994; Zlatanova and Leuba, 2003; Zlatanova et al., 1994). In contrast, in the DREEM images, the nucleosomes show regions of decreased intensity within the nucleosomal core particle, and these features are reproducible in multiple scans, scans at different angles, and in trace and retrace images (Figure S2B). Furthermore, multiple nucleosomes in individual DREEM images display DNA paths at different orientations (Figure S2). The decreased intensities indicate regions of weaker electrostatic interactions between the tip and sample, which likely results from neutralization of charge and possibly changes in capacitance associated with the interaction between the protein and DNA. Consistent with this suggestion, using these decreased intensities to trace the path of DNA on the histone yields a model in which the DNA wraps around the histone core (compare the models and images in Figure 2) (Luger et al., 1997; 2012). In the crystal structure, the DNA is wrapped around the histone 1.67 times (Luger et al., 1997; 2012), but nucleosomes exist in a dynamic equilibrium of states that have different extents of DNA wrapping (Luger et al., 2012). Consequently, one or two strands of DNA may be revealed in the DREEM images, depending on both the orientation of the nucleosomes on the surface and the extent of DNA wrapping. In addition, the ability to resolve two DNA strands wrapping around the histone will depend on the sharpness of the AFM tip and the quality of the DREEM signal. In half of the nucleosome images (n = 21 out of 41 nucleosomes), we observe one DNA strand wrapping around histones (Figures 2A, 2B, and S2), and in the other half (n = 20 out of 41 nucleosomes) we can visualize two DNA strands wrapping around the histone core, where cross-section analysis reveals two distinct peaks corresponding to DNA (Figures 2C and S2). The distance between the two peaks corresponding to two DNA double strands is 4.2 ± 0.8 nm, which is slightly larger than that seen in the crystal structure (~3 nm) (Luger et al., 1997). This difference is likely due to both different conformations of the nucleosomes on the surface and the limit of our resolution. In the images in which two DNA strands are seen, the tip was particularly sharp, as revealed by the width of the DNA in the topographic and DREEM images (e.g., Figure 2C). This result suggests that the spatial resolution of the DREEM images, like that of the topographic images, is limited by the tip size. Notably, it is possible to overlay the crystal structure of the nucleosome onto the DREEM image of the nucleosome showing two strands (Figure 2C). Taken together, these results demonstrate that DREEM can be a powerful method for resolving the path of DNA wrapped around proteins.

To further test the capability of DREEM for visualizing DNA contained within protein complexes, we imaged protein-DNA complexes involved in DNA MMR (Supplemental Experimental Procedures). In MMR, MutS homologs recognize DNA mismatches and subsequently form multimeric complexes with MutL homologs in the presence of ATP (Elez et al., 2012; Grilley et al., 1989; Hombauer et al., 2011; Kunkel and Erie, 2005, 2015; Schofield et al., 2001). MutS homologs are dimers with DNA binding and ATPase domains, and the DNA binding domains encircle and bend the DNA (Figure 3A) (Lamers et al., 2000; Obmolova et al., 2000; Warren et al., 2007). In addition, two MutS dimers can associate to form DNA loops (Allen et al., 1997; Jiang and Marszalek, 2011; Wang et al., 2003). Furthermore, in the presence of ATP, MutS homologs form a mobile clamp after mismatch recognition that can move away from the mismatch, which allows multiple proteins to load onto DNA containing a single mismatch (Cho et al., 2012; Gradia et al., 1999; Kunkel and Erie, 2015; Qiu et al., 2012). Topographic AFM images of *T. aquaticus* (*Taq*) MutS bound to a GT mismatch (Figure 3B) and two MutS dimers forming a DNA loop between the mismatch and a DNA end (Figure 3C) show the typical smooth peaks on the DNA corresponding to *Taq* MutS (Tessmer et al., 2008; Wang et al., 2003). In contrast, in the DREEM images (Figure 3) the ''peaks'' corresponding to the position of MutS show regions of decreased intensity, similar to our observations with nucleosomes (Figures 2 and S2). The regions of decreased intensity reveal the path of the DNA through MutS, which is hidden in the topographic AFM images. For example, in Figure 3B, MutS appears to be lying on its side (relative to model in Figure 3A) such that the bend in the DNA is clearly revealed. In this orientation, only a small amount of protein is on top of the DNA, allowing the complete path of the DNA to be visualized. In Figure 3C, the path of the DNA is partially obscured by MutS, which appears to be sitting upright on top of the DNA at the mismatch. As illustrated in the model, the DNA appears to come from underneath the protein (going from top to bottom of the image) and exit on the top (where the DNA can be clearly visualized exiting the protein), with the DNA bend potentially occurring perpendicular to the surface and hidden by the protein. After exiting the protein at the mismatch, the DNA loops back to interact with the second MutS bound at the end of the DNA. Images of multiple hMutSα proteins loaded onto DNA in the presence of ATP also clearly show the DNA passing through the proteins (Figure S3). Inspection of these and other images (not shown) suggests that the contrast between the DNA and protein in the DREEM images depends on how close the protein-DNA interaction site is to the tip. If the DNA is underneath a large amount of protein, then the electrostatic properties of the protein will likely screen out the effect of the DNA. This observation is similar to that seen with carbon nanotubes embedded in a polymer matrix, in which the contrast of the nanotubes decreases with increasing depth of the nanotubes in the matrix (Thompson et al., 2013). In addition to visualizing the DNA inside the complex, the DREEM data taken together with structural data on MutS (Obmolova et al., 2000) allow us to model the general orientation of the MutS dimers in the complexes (Figures 3B and 3C). The potential power of DREEM is revealed in the image of a large multiprotein complex of human MutSα and MutLα bound to DNA containing a GT

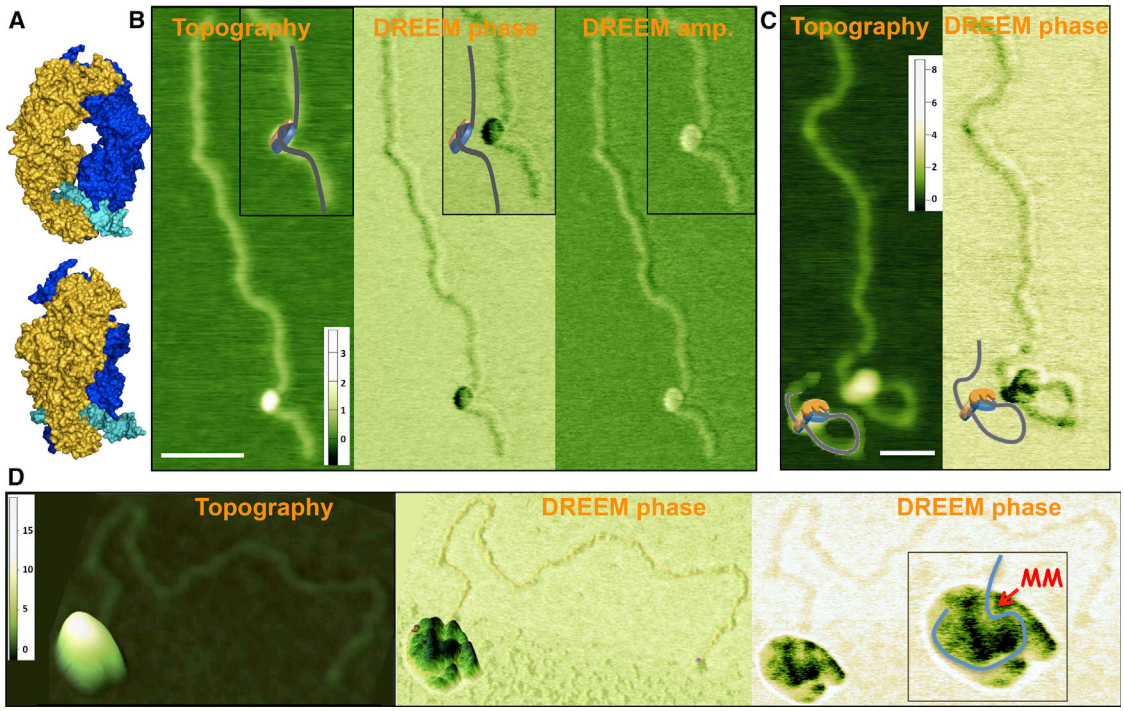

Figure 3. Topographic AFM and DREEM Images of Mismatch Repair Complexes on 2 kbp DNA Containing a GT Mismatch

(A) Space-filling model of the crystal structure of *Taq* MutS (generated from PDB: 1EWQ). Subunits A and B and the DNA are colored blue, gold, and cyan, respectively. MutS bends the DNA by ~60° as it passes through the DNA binding channel.

(B) AFM topographic (left) and DREEM-phase (center) and amplitude (right) images of a *Taq* MutS-DNA mismatch complex. Model of the complex is shown overlaid onto the AFM images and next to the phase images.

(C) AFM topographic (left) and DREEM-phase (right) images of two MutS dimers forming a loop in the DNA between the location of the mismatch (375 bp from one end) and DNA end. Model of the complex is shown overlaid onto the AFM images and next to the phase images. The model is based on the volume of the complex in the topographic image (consistent with two dimers), the location of the DNA in the DREEM image, as well as the crystal structure and the location of the tetramerization (two MutS dimers) interface (Groothuizen et al., 2013; Mendillo et al., 2007). A topographic surface plot of this image is shown in Figure 1.

(D) AFM topographic (left: surface plot) and DREEM-phase (middle: surface plot; right: top view) images of a large MutSα-MutLα-DNA complex containing ~10 proteins. The path of the DNA is identified as the regions with highest reduction of the magnitude of DREEM signals compared to protein alone and traced in the inset in blue. Interestingly, the DNA appears to be sharply bent after entering the complex at the expected position of the mismatch (MM). Z-scale bars are in nanometers for AFM images and arbitrary units for the DREEM images. See also Figure S3.

mismatch (Figure 3D). In the topographic image, a large protein complex is seen at the end of the DNA. This complex is one of the larger MutSα-MutLα complexes that we observe, and it was chosen to demonstrate the capability of DREEM for resolving DNA in large multiprotein-DNA complexes. A detailed analysis of the properties of MutSα and MutLα complexes is the focus of another manuscript. The volume of this complex is consistent with it containing ~10 proteins (Ratcliff and Erie, 2001). The length of the DNA that is not inside the protein complex is ~120 nm shorter than the expected length for 2 kbp DNA. Inspection of the DREEM amplitude and phase images reveals the path of the DNA in this large complex (Figure 3D). Including the DNA inside the proteins yields a DNA length that is within 5% of the expected length. These results suggest that DREEM may be a powerful tool for examining the path of DNA in large multiprotein-DNA complexes that may not be amenable to characterization by other techniques. In fact, the DNA path is often easier to discern in larger protein-DNA or multiprotein-DNA complexes because the DREEM signal of protein surrounding the DNA provides better contrast relative to DNA on the mica surface.

Limitations

Other than the requirement that the samples must be deposited on a surface to be imaged, which is common to all scanning probe microscopies, the primary limitation of DREEM relates to the use of highly doped silicon cantilevers. Although doped diamond-coated cantilevers (tip radius ~100 nm) and metal-coated cantilevers (tip radius ~30 nm) are typical choices for EFM imaging (Fumagalli et al., 2014), they are not sufficiently sharp to produce high-resolution images. Highly doped silicon cantilevers are sharp (5–8 nm) and sufficiently conductive for high-resolution topographic and DREEM imaging; however, the quality of the DREEM image appears to depend on the oxidation layers on the surface. The oxidation layer on the silicon cantilevers requires that the DC and AC biases be optimized for each cantilever. These differences in oxidation layers prevent quantitative comparison of the magnitudes of the DREEM signals collected with different tips, or the same tip after collecting a series of images. In addition, ~30% of prepared conductive silicon cantilevers do not generate sufficient contrast between the protein and DNA to allow us to discern paths of DNA in protein-DNA

complexes in DREEM images. Argon plasma cleaning of the cantilevers prior to use appears to improve their quality for DREEM imaging. Finally, the quality of the DREEM images degrades during imaging faster than that of the topographic images. Typically, ~10–12 high-quality DREEM images can be obtained from a single AFM tip.

Similar to conventional AFM imaging techniques, DREEM imaging can also experience tip artifacts, due to the asymmetry in the electric field between the AFM tip and sample surface. For example, in some cases, half-moon-like asymmetries, with one side of the DREEM signal consistently stronger than the other side, are seen in the same orientation for all complexes in a single DREEM image. As with tip artifacts in topographic images, these artifacts can be identified by the repetitive features in different molecules from the same image and by scanning at various angles.

A final limitation of DREEM is that it is currently limited to imaging in air. At present, we have not been able to identify operating parameters that allow contrast in aqueous environment. A few studies demonstrate EFM imaging of solid materials at low ionic strength using lift mode (Gramse et al., 2012; Johnson et al., 2003); however, the resolution and detection limit in these images appears low. It is likely that the electrostatic double layer significantly damps the DREEM signals from proteins and DNA in electrolyte solutions.

Conclusions

In summary, while the paths of DNA are hidden in protein complexes in traditional microscopy imaging techniques, such as AFM and EM imaging, DREEM allows the visualization of the conformation of DNA within individual protein-DNA complexes. In addition to the studies presented here, DREEM also has been employed to visualize DNA conformations within telomere binding proteins (Benarroch-Popivker et al., 2016; P.K., D.W., L. Lin, P. Countryman, K.C.B., D.A.E., R. Riehn, P.L. Opresko, and H.W., unpublished data). Taken together, the capability of DREEM to detect very small changes in electrostatic force gradient with high resolution makes it a powerful tool for characterizing the structure of protein-DNA complexes at the single-molecule level. It will be especially useful for characterizing protein-DNA complexes with long length scales and those that result in heterogeneous populations of proteins on the DNA. Furthermore, a growing area in structural biology is the combination of atomic-resolution crystal structures with lower-resolution data from small-angle X-ray scattering, EM, and AFM to generate atomic-level structures of complex assemblies and conformationally flexible proteins (Bustamante et al., 1994; Erie et al., 1994; Griffith, 2013; Griffith and Christiansen, 1978; Hennig and Sattler, 2014; Hura et al., 2013a, 2013b; Janićijević et al., 2003; Lohr et al., 2007; Lyubchenko et al., 2001; Moreno-Herrero et al., 2005; Sanchez et al., 2013; Trinh et al., 2012; Villarreal and Stewart, 2014; Wanner and Schroeder-Reiter, 2008; Williams et al., 2014; Yang et al., 2003; Yeh et al., 2012). DREEM has the capability to significantly increase the constraints on the possible orientations of proteins in multiprotein assemblies on DNA, as demonstrated by our ability to dock the crystal structure of the nucleosome into a subset of the images. In addition, DREEM allows the path of DNA to be resolved in large heterogeneous multi-protein-DNA complexes. It also will be applicable for characterizing the electrostatic properties of other biological specimens, such as viruses and membranes, as well as non-biological samples. With sharper tips and further refinement of the technique, it is highly likely that the resolution can be further increased in the future. Finally, with the addition of only two components (a function generator and a lock-in amplifier, Figure 1), DREEM can be implemented on many of the commercially available AFMs, making it readily available to many labs.

EXPERIMENTAL PROCEDURES

Instrument Design

Our experimental setup for simultaneous AFM and DREEM is described in Figure 1. In our setup, we apply an AC bias at the first overtone (ω_2) and monitor the vibration amplitude (A_{ω_2}) and phase (φ_{ω_2}) as a function of position, while simultaneously collecting the topographic image at the fundamental frequency (ω_1).

The detailed methods for conductive cantilever preparation, substrate grounding, selection of imaging conditions, sample preparation, deposition, and analysis are described in the Supplemental Experimental Procedures.

SUPPLEMENTAL INFORMATION

Supplemental Information includes the Theoretical Basis of DREEM, Supplemental Experimental Procedures, and three figures and can be found with this article online at http://dx.doi.org/10.1016/j.molcel.2015.12.012.

AUTHOR CONTRIBUTIONS

D.W. and D.A.E. invented the DREEM method. K.C.B. prepared human mismatch repair protein-DNA samples. D.W., P.K., Z.M.L., H.W., and D.A.E. designed and conducted experiments, analyzed data, and wrote the manuscript.

ACKNOWLEDGMENTS

We would like to thank James Jorgenson for the use of the lock-in amplifier, Peggy Hsieh for providing human MutSα and MutLα proteins, and Elizabeth Sacho and Keith Weninger for helpful discussions and critical reading of the manuscript. This work was supported by National Institutes of Health grant R01 GM079480 (D.A.E.), R00 ES016758 (H.W.), R01 GM107559 (H.W.), P30ES025128 (H.W.), and NCSU start-up fund (H.W.). D.A.E. and D.W. have a patent pending on the DREEM technique.

Received: June 1, 2015
Revised: October 14, 2015
Accepted: December 2, 2015
Published: January 7, 2016

REFERENCES

Albrecht, T.R., Grütter, P., Horne, D., and Rugar, D. (1991). Frequency modulation detection using high-Q cantilevers for enhanced force microscope sensitivity. J. Appl. Physiol. *69*, 668–673.

Allen, D.J., Makhov, A., Grilley, M., Taylor, J., Thresher, R., Modrich, P., and Griffith, J.D. (1997). MutS mediates heteroduplex loop formation by a translocation mechanism. EMBO J. *16*, 4467–4476.

Barth, C., Foster, A.S., Henry, C.R., and Shluger, A.L. (2011). Recent trends in surface characterization and chemistry with high-resolution scanning force methods. Adv. Mater. *23*, 477–501.

Bazett-Jones, D.P., Mendez, E., Czarnota, G.J., Ottensmeyer, F.P., and Allfrey, V.G. (1996). Visualization and analysis of unfolded nucleosomes associated with transcribing chromatin. Nucleic Acids Res. *24*, 321–329.

Benarroch-Popivker, D., Pisano, S., Mendez-Bermudez, A., Lototska, L., Kaur, P., Bauwens, S., Djerbi, N., Latrick, C.M., Fraisier, V., Pei, B., et al. (2016). TRF2-Mediated Control of Telomere DNA Topology as a Mechanism for Chromosome Chromosome-End Protection as a Mechanism for Chromosome Chromosome-End Protection. Mol Cell *61*, this issue, 274–286.

Bonnell, D.A., and Kalinin, S.V. (2001). Local Polarization, Charge Compensation, and Chemical Interactions on Ferroelectric Surfaces: a Route Toward New Nanostructures. MRS Proceedings *688*.

Brown, A., Amunts, A., Bai, X.C., Sugimoto, Y., Edwards, P.C., Murshudov, G., Scheres, S.H., and Ramakrishnan, V. (2014). Structure of the large ribosomal subunit from human mitochondria. Science *346*, 718–722.

Bustamante, C., Erie, D.A., and Keller, D. (1994). Biochemical and structural applications of scanning force microscopy. Curr. Opin. Struct. Biol. *4*, 750–760.

Bustamante, C., Zuccheri, G., Leuba, S.H., Yang, G., and Samori, B. (1997). Visualization and analysis of chromatin by scanning force microscopy. Methods *12*, 73–83.

Cho, W.-K., Jeong, C., Kim, D., Chang, M., Song, K.-M., Hanne, J., Ban, C., Fishel, R., and Lee, J.-B. (2012). ATP alters the diffusion mechanics of MutS on mismatched DNA. Structure *20*, 1264–1274.

Choi, K.J., Biegalski, M., Li, Y.L., Sharan, A., Schubert, J., Uecker, R., Reiche, P., Chen, Y.B., Pan, X.Q., Gopalan, V., et al. (2004). Enhancement of ferroelectricity in strained BaTiO3 thin films. Science *306*, 1005–1009.

Cleveland, J., Anczykowski, B., Schmid, A., and Elings, V. (1998). Energy dissipation in tapping-mode atomic force microscopy. Appl. Phys. Lett. *72*, 2613.

Colchero, J., Gil, A., and Baró, A. (2001). Resolution enhancement and improved data interpretation in electrostatic force microscopy. Phys. Rev. B *64*, 245403.

Ding, X.D., An, J., Xu, J.B., Li, C., and Zeng, R.Y. (2009). Improving lateral resolution of electrostatic force microscopy by multifrequency method under ambient conditions. Appl. Phys. Lett. *94*, 223109.

Elez, M., Radman, M., and Matic, I. (2012). Stoichiometry of MutS and MutL at unrepaired mismatches in vivo suggests a mechanism of repair. Nucleic Acids Res. *40*, 3929–3938.

Erie, D.A., Yang, G., Schultz, H.C., and Bustamante, C. (1994). DNA bending by Cro protein in specific and nonspecific complexes: implications for protein site recognition and specificity. Science *266*, 1562–1566.

Fernández, I.S., Bai, X.C., Hussain, T., Kelley, A.C., Lorsch, J.R., Ramakrishnan, V., and Scheres, S.H. (2013). Molecular architecture of a eukaryotic translational initiation complex. Science *342*, 1240585.

Fumagalli, L., Edwards, M.A., and Gomila, G. (2014). Quantitative electrostatic force microscopy with sharp silicon tips. Nanotechnology *25*, 495701.

Giessibl, F.J. (1995). Atomic resolution of the silicon (111)-(7x7) surface by atomic force microscopy. Science *267*, 68–71.

Glatzel, T. (2003). Amplitude or frequency modulation-detection in Kelvin probe force microscopy. Appl. Surf. Sci. *210*, 84–89.

Gradia, S., Subramanian, D., Wilson, T., Acharya, S., Makhov, A., Griffith, J., and Fishel, R. (1999). hMSH2-hMSH6 forms a hydrolysis-independent sliding clamp on mismatched DNA. Mol. Cell *3*, 255–261.

Gramse, G., Gomila, G., and Fumagalli, L. (2012). Quantifying the dielectric constant of thick insulators by electrostatic force microscopy: effects of the microscopic parts of the probe. Nanotechnology *23*, 205703.

Griffith, J.D. (2013). Many ways to loop DNA. J. Biol. Chem. *288*, 29724–29735.

Griffith, J.D., and Christiansen, G. (1978). Electron microscope visualization of chromatin and other DNA-protein complexes. Annu. Rev. Biophys. Bioeng. *7*, 19–35.

Grilley, M., Welsh, K.M., Su, S.S., and Modrich, P. (1989). Isolation and characterization of the Escherichia coli mutL gene product. J. Biol. Chem. *264*, 1000–1004.

Groothuizen, F.S., Fish, A., Petoukhov, M.V., Reumer, A., Manelyte, L., Winterwerp, H.H., Marinus, M.G., Lebbink, J.H., Svergun, D.I., Friedhoff, P., and Sixma, T.K. (2013). Using stable MutS dimers and tetramers to quantitatively analyze DNA mismatch recognition and sliding clamp formation. Nucleic Acids Res. *41*, 8166–8181.

Gruverman, A., Wu, D., Lu, H., Wang, Y., Jang, H.W., Folkman, C.M., Zhuravlev, M.Y., Felker, D., Rzchowski, M., Eom, C.B., and Tsymbal, E.Y. (2009). Tunneling electroresistance effect in ferroelectric tunnel junctions at the nanoscale. Nano Lett. *9*, 3539–3543.

He, Y., Fang, J., Taatjes, D.J., and Nogales, E. (2013). Structural visualization of key steps in human transcription initiation. Nature *495*, 481–486.

Hennig, J., and Sattler, M. (2014). The dynamic duo: combining NMR and small angle scattering in structural biology. Protein Sci. *23*, 669–682.

Hombauer, H., Campbell, C.S., Smith, C.E., Desai, A., and Kolodner, R.D. (2011). Visualization of eukaryotic DNA mismatch repair reveals distinct recognition and repair intermediates. Cell *147*, 1040–1053.

Hoummady, M., and Farnault, E. (1998). Enhanced sensitivity to force gradients by using higher flexural modes of the atomic force microscope cantilever. Applied Physics A: Materials Science & Processing *66*, 361–364.

Hura, G.L., Budworth, H., Dyer, K.N., Rambo, R.P., Hammel, M., McMurray, C.T., and Tainer, J.A. (2013a). Comprehensive macromolecular conformations mapped by quantitative SAXS analyses. Nat. Methods *10*, 453–454.

Hura, G.L., Tsai, C.L., Claridge, S.A., Mendillo, M.L., Smith, J.M., Williams, G.J., Mastroianni, A.J., Alivisatos, A.P., Putnam, C.D., Kolodner, R.D., and Tainer, J.A. (2013b). DNA conformations in mismatch repair probed in solution by X-ray scattering from gold nanocrystals. Proc. Natl. Acad. Sci. USA *110*, 17308–17313.

Janićijević, A., Ristic, D., and Wyman, C. (2003). The molecular machines of DNA repair: scanning force microscopy analysis of their architecture. J. Microsc. *212*, 264–272.

Jiang, Y., and Marszalek, P.E. (2011). Atomic force microscopy captures MutS tetramers initiating DNA mismatch repair. EMBO J. *30*, 2881–2893.

Johnson, A.S., Nehl, C.L., Mason, M.G., and Hafner, J.H. (2003). Fluid Electric Force Microscopy for Charge Density Mapping in Biological Systems. Langmuir *19*, 10007–10010.

Kikukawa, A., Hosaka, S., and Imura, R. (1996). Vacuum compatible high-sensitive Kelvin probe force microscopy. Rev. Sci. Instrum. *67*, 1463–1467.

Kokavecz, J., and Mechler, A. (2008). Spring constant of microcantilevers in fundamental and higher eigenmodes. Phys. Rev. B *78*, 172101.

Kunkel, T.A., and Erie, D.A. (2005). DNA mismatch repair. Annu. Rev. Biochem. *74*, 681–710.

Kunkel, T.A., and Erie, D.A. (2015). Eukaryotic Mismatch Repair in Relation to DNA Replication. Annu. Rev. Genet. *49*, 291–313.

Lamers, M.H., Perrakis, A., Enzlin, J.H., Winterwerp, H.H., de Wind, N., and Sixma, T.K. (2000). The crystal structure of DNA mismatch repair protein MutS binding to a G x T mismatch. Nature *407*, 711–717.

Lei, C., Das, A., Elliott, M., and Macdonald, J.E. (2004). Quantitative electrostatic force microscopy-phase measurements. Nanotechnology *15*, 627.

Leung, C., Maradan, D., Kramer, A., Howorka, S., Mesquida, P., and Hoogenboom, B.W. (2010). Improved Kelvin probe force microscopy for imaging individual DNA molecules on insulating surfaces. Appl. Phys. Lett. *97*, 203703.

Lohr, D., Bash, R., Wang, H., Yodh, J., and Lindsay, S. (2007). Using atomic force microscopy to study chromatin structure and nucleosome remodeling. Methods *41*, 333–341.

Luger, K., Mäder, A.W., Richmond, R.K., Sargent, D.F., and Richmond, T.J. (1997). Crystal structure of the nucleosome core particle at 2.8 A resolution. Nature *389*, 251–260.

Luger, K., Dechassa, M.L., and Tremethick, D.J. (2012). New insights into nucleosome and chromatin structure: an ordered state or a disordered affair? Nat. Rev. Mol. Cell Biol. *13*, 436–447.

Luijsterburg, M.S., von Bornstaedt, G., Gourdin, A.M., Politi, A.Z., Moné, M.J., Warmerdam, D.O., Goedhart, J., Vermeulen, W., van Driel, R., and Höfer, T. (2010). Stochastic and reversible assembly of a multiprotein DNA repair

complex ensures accurate target site recognition and efficient repair. J. Cell Biol. *189*, 445–463.

Lyubchenko, Y.L. (2014). Nanoscale Nucleosome Dynamics Assessed with Time-lapse AFM. Biophys. Rev. *6*, 181–190.

Lyubchenko, Y.L., Gall, A.A., and Shlyakhtenko, L.S. (2001). Atomic force microscopy of DNA and protein-DNA complexes using functionalized mica substrates. Methods Mol. Biol. *148*, 569–578.

Maletta, M., Orlov, I., Roblin, P., Beck, Y., Moras, D., Billas, I.M., and Klaholz, B.P. (2014). The palindromic DNA-bound USP/EcR nuclear receptor adopts an asymmetric organization with allosteric domain positioning. Nat. Commun. *5*, 4139.

Martin, Y., Williams, C.C., and Wickramasinghe, H.K. (1987). Atomic force microscope–force mapping and profiling on a sub 100-Å scale. J. Appl. Physiol. *61*, 4723–4729.

Martínez, N.F., and García, R. (2006). Measuring phase shifts and energy dissipation with amplitude modulation atomic force microscopy. Nanotechnology *17*, S167–S172.

Martínez, N.F., Lozano, J.R., Herruzo, E.T., Garcia, F., Richter, C., Sulzbach, T., and Garcia, R. (2008). Bimodal atomic force microscopy imaging of isolated antibodies in air and liquids. Nanotechnology *19*, 384011.

Melitz, W., Shen, J., Kummel, A.C., and Lee, S. (2011). Kelvin probe force microscopy and its application. Surf. Sci. Rep. *66*, 1–27.

Mendillo, M.L., Putnam, C.D., and Kolodner, R.D. (2007). Escherichia coli MutS tetramerization domain structure reveals that stable dimers but not tetramers are essential for DNA mismatch repair in vivo. J. Biol. Chem. *282*, 16345–16354.

Mikamo-Satoh, E., Yamada, F., Takagi, A., Matsumoto, T., and Kawai, T. (2009). Electrostatic force microscopy: imaging DNA and protein polarizations one by one. Nanotechnology *20*, 145102.

Miyata, T., Suzuki, H., Oyama, T., Mayanagi, K., Ishino, Y., and Morikawa, K. (2005). Open clamp structure in the clamp-loading complex visualized by electron microscopic image analysis. Proc. Natl. Acad. Sci. USA *102*, 13795–13800.

Moreno-Herrero, F., de Jager, M., Dekker, N.H., Kanaar, R., Wyman, C., and Dekker, C. (2005). Mesoscale conformational changes in the DNA-repair complex Rad50/Mre11/Nbs1 upon binding DNA. Nature *437*, 440–443.

Nonnenmacher, M., O'Boyle, M.P., and Wickramasinghe, H.K. (1991). Kelvin probe force microscopy. Appl. Phys. Lett. *58*, 2921.

Obmolova, G., Ban, C., Hsieh, P., and Yang, W. (2000). Crystal structures of mismatch repair protein MutS and its complex with a substrate DNA. Nature *407*, 703–710.

Orlova, E.V., and Saibil, H.R. (2010). Methods for three-dimensional reconstruction of heterogeneous assemblies. Methods Enzymol. *482*, 321–341.

Qiu, R., DeRocco, V.C., Harris, C., Sharma, A., Hingorani, M.M., Erie, D.A., and Weninger, K.R. (2012). Large conformational changes in MutS during DNA scanning, mismatch recognition and repair signalling. EMBO J. *31*, 2528–2540.

Ratcliff, G.C., and Erie, D.A. (2001). A novel single-molecule study to determine protein–protein association constants. J. Am. Chem. Soc. *123*, 5632–5635.

Rezek, B. (2005). Atomic and Kelvin force microscopy applied on hydrogenated diamond surfaces. New Diam Front C Tech *15*, 275–295.

Rodríguez, T.R., and García, R. (2004). Compositional mapping of surfaces in atomic force microscopy by excitation of the second normal mode of the microcantilever. Appl. Phys. Lett. *84*, 449.

Sanchez, H., Kertokalio, A., van Rossum-Fikkert, S., Kanaar, R., and Wyman, C. (2013). Combined optical and topographic imaging reveals different arrangements of human RAD54 with presynaptic and postsynaptic RAD51-DNA filaments. Proc. Natl. Acad. Sci. USA *110*, 11385–11390.

Schofield, M.J., Nayak, S., Scott, T.H., Du, C., and Hsieh, P. (2001). Interaction of Escherichia coli MutS and MutL at a DNA mismatch. J. Biol. Chem. *276*, 28291–28299.

Stark, R.W., Drobek, T., and Heckl, W.M. (1999). Tapping-mode atomic force microscopy and phase-imaging in higher eigenmodes. Appl. Phys. Lett. *74*, 3296–3298.

Stark, R.W., Naujoks, N., and Stemmer, A. (2007). Multifrequency electrostatic force microscopy in the repulsive regime. Nanotechnology *18*, 065502.

Swygert, S.G., Manning, B.J., Senapati, S., Kaur, P., Lindsay, S., Demeler, B., and Peterson, C.L. (2014). Solution-state conformation and stoichiometry of yeast Sir3 heterochromatin fibres. Nat. Commun. *5*, 4751.

Tamayo, J. (2005). Study of the noise of micromechanical oscillators under quality factor enhancement via driving force control. J. Appl. Physiol. *97*, 044903.

Tessmer, I., Yang, Y., Zhai, J., Du, C., Hsieh, P., Hingorani, M.M., and Erie, D.A. (2008). Mechanism of MutS searching for DNA mismatches and signaling repair. J. Biol. Chem. *283*, 36646–36654.

Thompson, H.T., Barroso-Bujans, F., Herrero, J.G., Reifenberger, R., and Raman, A. (2013). Subsurface imaging of carbon nanotube networks in polymers with DC-biased multifrequency dynamic atomic force microscopy. Nanotechnology *24*, 135701.

Trinh, M.H., Odorico, M., Pique, M.E., Teulon, J.M., Roberts, V.A., Ten Eyck, L.F., Getzoff, E.D., Parot, P., Chen, S.W., and Pellequer, J.L. (2012). Computational reconstruction of multidomain proteins using atomic force microscopy data. Structure *20*, 113–120.

Trithaveesak, O., Schubert, J., and Buchal, C. (2005). Ferroelectric properties of epitaxial BaTiO3 thin films and heterostructures on different substrates. J. Appl. Physiol. *98*, 114101.

Villarreal, S.A., and Stewart, P.L. (2014). CryoEM and image sorting for flexible protein/DNA complexes. J. Struct. Biol. *187*, 76–83.

Wang, H., Bash, R., Yodh, J.G., Hager, G.L., Lohr, D., and Lindsay, S.M. (2002). Glutaraldehyde modified mica: a new surface for atomic force microscopy of chromatin. Biophys. J. *83*, 3619–3625.

Wang, H., Yang, Y., Schofield, M.J., Du, C., Fridman, Y., Lee, S.D., Larson, E.D., Drummond, J.T., Alani, E., Hsieh, P., and Erie, D.A. (2003). DNA bending and unbending by MutS govern mismatch recognition and specificity. Proc. Natl. Acad. Sci. USA *100*, 14822–14827.

Wanner, G., and Schroeder-Reiter, E. (2008). Scanning electron microscopy of chromosomes. Methods Cell Biol. *88*, 451–474.

Warren, J.J., Pohlhaus, T.J., Changela, A., Iyer, R.R., Modrich, P.L., and Beese, L.S. (2007). Structure of the human MutSalpha DNA lesion recognition complex. Mol. Cell *26*, 579–592.

Williams, G.J., Hammel, M., Radhakrishnan, S.K., Ramsden, D., Lees-Miller, S.P., and Tainer, J.A. (2014). Structural insights into NHEJ: building up an integrated picture of the dynamic DSB repair super complex, one component and interaction at a time. DNA Repair (Amst.) *17*, 110–120.

Yang, G., Leuba, S.H., Bustamante, C., Zlatanova, J., and van Holde, K. (1994). Role of linker histones in extended chromatin fibre structure. Nat. Struct. Biol. *1*, 761–763.

Yang, Y., Wang, H., and Erie, D.A. (2003). Quantitative characterization of biomolecular assemblies and interactions using atomic force microscopy. Methods *29*, 175–187.

Yeh, J.I., Levine, A.S., Du, S., Chinte, U., Ghodke, H., Wang, H., Shi, H., Hsieh, C.L., Conway, J.F., Van Houten, B., and Rapić-Otrin, V. (2012). Damaged DNA induced UV-damaged DNA-binding protein (UV-DDB) dimerization and its roles in chromatinized DNA repair. Proc. Natl. Acad. Sci. USA *109*, E2737–E2746.

Ziegler, D., Rychen, J., Naujoks, N., and Stemmer, A. (2007). Compensating electrostatic forces by single-scan Kelvin probe force microscopy. Nanotechnology *18*, 225505.

Zlatanova, J., and Leuba, S.H. (2003). Chromatin fibers, one-at-a-time. J. Mol. Biol. *331*, 1–19.

Zlatanova, J., Leuba, S.H., Yang, G., Bustamante, C., and van Holde, K. (1994). Linker DNA accessibility in chromatin fibers of different conformations: a reevaluation. Proc. Natl. Acad. Sci. USA *91*, 5277–5280.

Molecular Cell, Volume *61*

Supplemental Information

Visualizing the Path of DNA through Proteins Using DREEM Imaging

Dong Wu, Parminder Kaur, Zimeng M. Li, Kira C. Bradford, Hong Wang, and Dorothy A. Erie

A

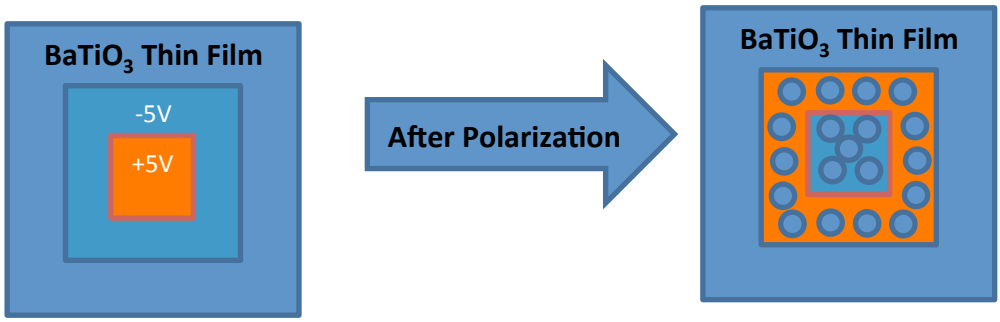

B

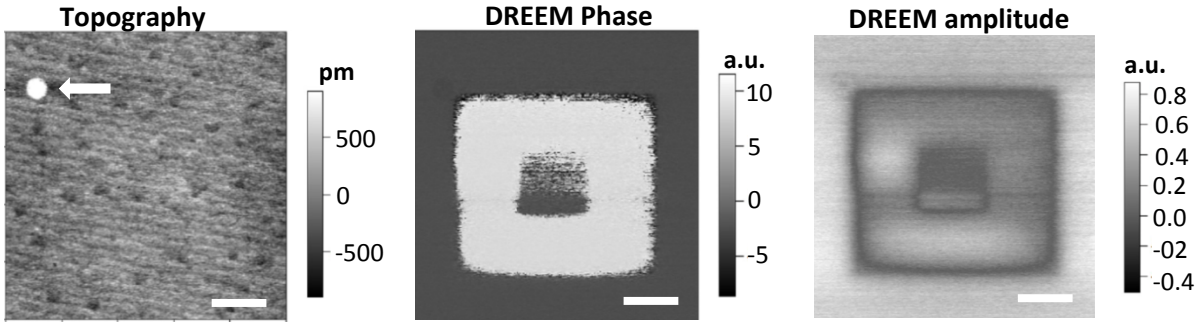

Figure S1, related to Figure 1. Topographic and DREEM images of a polarized $BaTiO_3$ (BTO) thin film. (A) Schematic showing the generation of a surface pattern with different polarization states on a BTO film. External electric fields (-5V DC bias for the larger area followed by +5V bias for the smaller area) are applied through a conductive AFM cantilever. The charge density on the BTO thin film after polarization was estimated to be approximately 2 electrons/nm^2. (B) Topographic (left), DREEM phase (middle), and DREEM amplitude (right) images of the polarized areas on the BTO thin film. The DREEM phase and amplitude images directly reveal the pattern of charged areas, without any detectable crosstalk into the topographic channel. In addition, the large contaminant particle seen in the topographic image (white arrow) is not seen in the DREEM images, indicating that there is no crosstalk of the topographic signal into the DREEM signals. The XY scale bars are 1 μm.

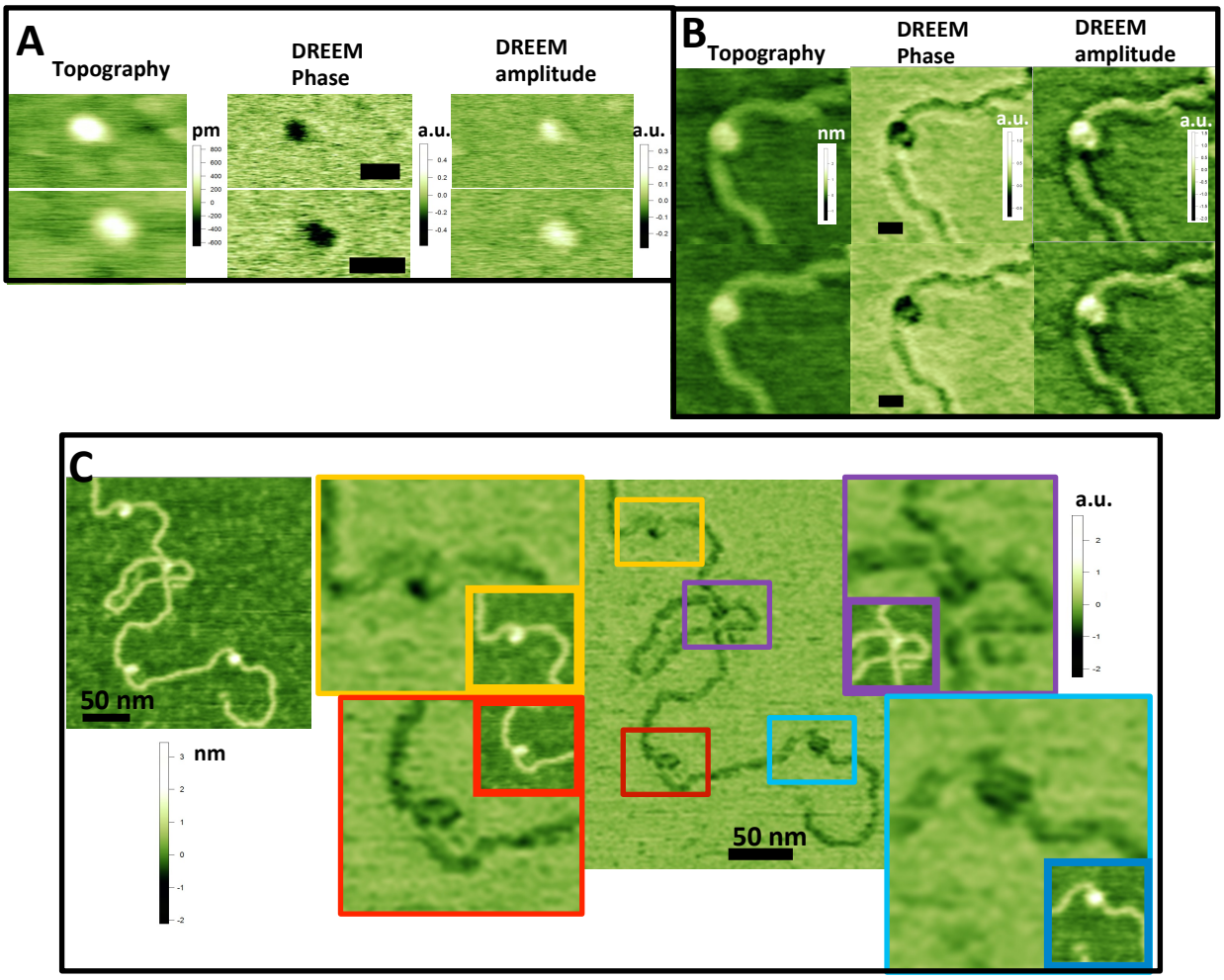

Figure S2, related to Figure 2. Additional DREEM Images of histone alone and nucleosomes. (A) DREEM images of histone proteins alone in the absence of DNA. Topographic (*left panels*), DREEM phase (*middle panels*), and DREEM amplitude (*right panels*) images of two individual histone proteins (top and bottom panels). (B) Repeated scans (*top panels*) and retrace images (*bottom panels*) of the nucleosome shown in Figure 2B. The topographic (*left panels*), DREEM phase (*middle panels*), and DREEM amplitude images (*right panels)* demonstrate the reproducibility of DREEM imaging. The XY scale bars are 20 nm. (C) DREEM imaging reveals DNA paths on multiple nucleosomes in individual images. *Left panel:* The topographic image. *Right panel*: A DREEM phase image of the same DNA molecule with multiple nucleosomes (*middle image*). Zoomed in areas with individual nucleosomes are shown surrounding the full image. Each nucleosome is identified by the matching color outlining the nucleosome molecules in the middle image. The inserts in the zoomed-in images show the corresponding topographic images (not to scale). The DNA paths revealed in DREEM images are at different orientations, ruling out the possibility that the signals consistent with DNA paths are due to scanning artefacts.

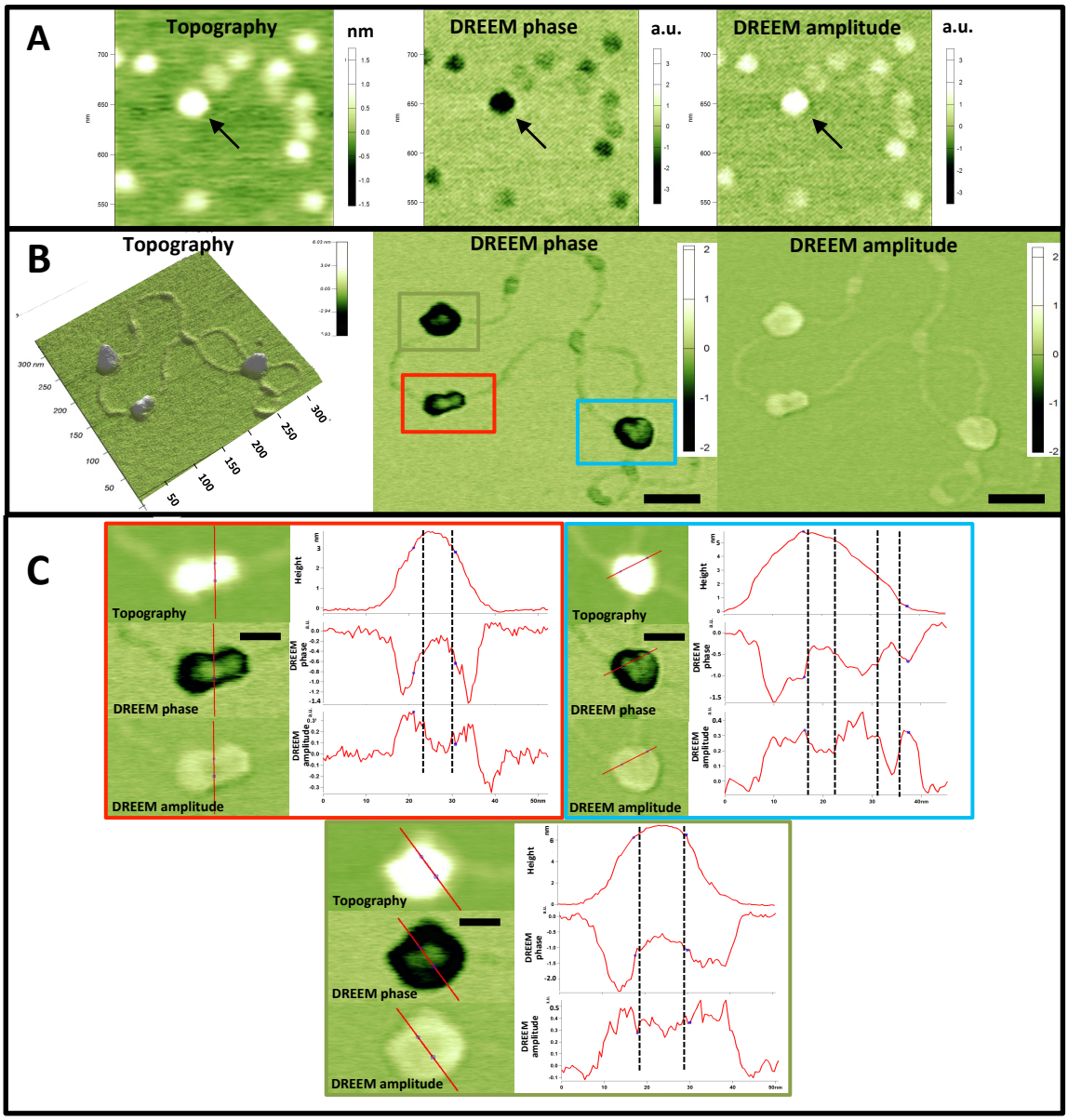

Figure S3, related to Figure 3. DREEM imaging reveals the path of the DNA in hMutSα mobile clamp complexes loaded onto a circular DNA substrate (4 kbp) containing two GT mismatches 2 kbp apart. (A) Topographic (*left*), DREEM phase (*middle*), and DREEM amplitude (*right*) images of a sample containing both hMutLα, which adopts multiple conformations (Sacho *et al*. *Mol Cell* 2008, 29:112-21), and hMutSα without DNA (hMutSα MW=257 kDa; hMutLα MW=180 kDa). The larger protein is hMutSα (identified by arrow). (B) Topographic (left), DREEM phase (middle), and DREEM amplitude (right) of multiple hMutSα sliding clamps formed by incubating 125 nM hMutSα and 1 mM ATP with the mismatch containing DNA. Based on the volume of the complexes in the topographic images, each of the complexes (in boxed regions) contain two or more hMutSα proteins. The scale bars are 50 nm. (C) Zoomed-in images showing the cross-section analysis of the hMutSα-DNA complexes in the boxed regions in B. The scale bars are 20 nm. The pairs of perpendicular lines on the section plots indicate the positions of the DNA strands. In the zoomed-in image in C (top left) (as well as in the overview image in B) two MutSα proteins can clearly be seen adjacent to one another on the DNA. In C (top right), the MutSα complex is interacting with two DNA stands, and the two individual duplex DNA strands can be clearly seen in the DREEM images and the cross-section analysis. Only DREEM images, but not topographic images reveal the DNA in hMutSα-DNA complexes.

Supplemental Information

Theoretical basis of DREEM measurements

As demonstrated below, because we are monitoring very small changes in surface potential on a modestly charged surface (mica), $\Delta A_{\omega_2}(x,y)$ will be dominated by changes in the force gradient, with only small contributions from the force. This method is similar to amplitude slope detection method used to monitor the atomic force gradient in topographic AFM images (Martin et al., 1987).

Because the AC bias is applied at the first overtone frequency (ω_2), the applied force induces a vibration, with a free amplitude (assuming no dampening)

$$A_{0,\omega_2} = \left(Q_2 \middle/ k_2\right) F_{\omega_2} = a\left(Q_2 \middle/ k_2\right)\frac{\partial C}{\partial z}(\Delta\phi_{TS} - V_{DC})V_{AC},$$

where Q_2 and k_2 are the quality factor and effective spring constant, respectively, of the first overtone of the cantilever, and *a* is a constant that depends on the tip radius, and tip-sample separation (García and Perez, 2002; Nonnenmacher et al., 1991; Rast et al., 2000). In addition, the force gradient, *F′*, changes the effective spring constant of the cantilever and shifts its first overtone frequencies by

$$\Delta\omega_2 = \omega_2 F' \middle/ 2k_c$$

where k_c is the spring constant of the cantilever (which is equal to k_1, the spring constant of ω_1) (Albrecht et al., 1991; Hoummady and Farnault, 1998; Martin et al., 1987), thereby reducing the vibration amplitude at ω_2 to

$$A_{\omega_2} \approx A_{0,\omega_2}\left[1 + b\left(Q_2 \middle/ k_c\right)F'\right]$$

This approximation assumes that the applied force is slightly off the resonance frequency on the side of the resonance peak, where the slope of the peak is maximum and $b = 2/3\sqrt{3}$ (Martin et al., 1987). Notably, the frequency shift and therefore the change in amplitude depend on both the static and dynamic components of the electrostatic force gradient (*i.e.*, F'_{DC} and F'_{ω_2}; eq. 1 & 2) (García and Perez, 2002; Takagi et al., 2009).

Because we are operating in intermittent contact, the force gradient (F'_a) due to repulsive atomic interactions is significantly greater than that due to the attractive electrostatic interactions (F'_{el}) (Hong et al., 1998; Hong et al., 1999); therefore, $\Delta\omega_2 > 0$. (We verified that $\Delta\omega_2 > 0$ in our experiments by monitoring the vibration amplitude as a function of the AC bias frequency.) Under our imaging conditions, A_{ω_2} is ~1/2 A_{0,ω_2} after engaging in repulsive mode. During scanning, however, F'_a should be constant because the topographic signal at ω_1 maintains a constant atomic force gradient, and therefore, changes in $\Delta\omega_2(x,y)$ will be dominated by F'_{el}. In addition, because $F'_a >> F'_{DC}$, F'_{DC} does not significantly contribute to the signal at ω_1. Consequently, the static electrical force gradient does not affect the topographic image, and therefore, F'_{DC} is not maintained constant during imaging and will contribute to the signal at ω_2. We confirmed that F'_{DC} does not affect the topographic images by turning the modulated bias voltage on and off while scanning.

Assuming that the atomic force gradient is constant as a function of x,y position of the tip, the change in A_{ω_2} ($\Delta A_{\omega_2}(x,y)$) due to changes in the electrostatic force and force gradient associated with a change in position from (x_1,y_1) to (x_2,y_2) on the surface is approximately

$$\Delta A_{\omega_2}(x,y) \approx \left(Q_2/k_2\right)\left[\Delta F_{\omega_2,el}(x,y) + b\left(Q_2/k_c\right)\Delta(F_{\omega_2,el}(x,y)F'_{el}(x,y))\right]$$

$$\Delta A_{\omega_2}(x,y) \approx \left(Q_2/k_2\right)\left(\Delta F_{\omega_2,el}(x,y) + b\left(Q_2/k_c\right)\left\{\left[F_{\omega_2,el}(x_1,y_1) + \Delta F_{\omega_2,el}(x,y)\right]F_{el}^{'}(x_2,y_2) - F_{\omega_2,el}(x_1,y_1)F_{el}^{'}(x_1,y_1)\right\}\right)$$

For small changes in surface potential [$\Delta\psi(x,y)$] or capacitance, such as those in the current experiments where $\Delta\psi(x,y)$ and capacitance changes are very small (only the difference in potential and/or capacitance between the mica substrate and the deposited protein and DNA molecules), $\Delta F_{\omega_2,el}(x,y) << F_{\omega_2,el}$ and

$$\Delta A_{\omega_2}(x,y) \approx \left(Q_2/k_2\right)\left(\Delta F_{\omega_2,el}(x,y) + b\left(Q_2/k_c\right)F_{\omega_2,el}\Delta F_{el}^{'}(x,y)\right)$$

Because $F_{\omega_2,el}$ is sensitive to electrostatic potential over a greater distance than $F_{el}^{'}$, the tip cone and the cantilever, as well as the tip apex, make contributions to $F_{\omega_2,el}(x,y)$, and therefore, $F_{\omega_2,el}(x,y)$ will be averaged over a greater area of the sample than $F_{el}^{'}(x,y)$ (Colchero et al., 2001; Ding et al., 2009; Giessibl, 1995; Gil et al., 2003; Glatzel, 2003; Martin et al., 1987; Tevaarwerk et al., 2005). Consequently, for small changes in capacitance and surface potential [*i.e.*, $\Delta\psi(x,y) << (\Delta\phi_{TS}-V_{DC})$] over an area similar to the tip radius, $F_{\omega_2,el}(x,y)$ may be relatively constant. If the force is approximately constant as a function of position then

$$\Delta A_{\omega_2}(x,y) \approx b\left(Q_2^2/k_c k_2\right)F_{\omega_2,el}\Delta F_{el}^{'}(x,y)$$

and only the force gradient contributes to $\Delta A_{\omega_2}(x,y)$. (For the cantilevers used in our experimental setup, $k_c \approx 2.8$ N/m, $k_2 \approx 110$ N/m, $Q_1 \approx 170$, and $Q_2 \approx 500$.). Because $\Delta\psi << (\Delta\phi_{TS}-V_{DC})$ for proteins and DNA deposited on mica (Leung et al., 2009; Leung et al., 2010), $\Delta A_{\omega_2}(x,y)$ is dominated by $F_{el}^{'}$.

Supplemental Experimental Procedures

Conductive cantilever preparation

To obtain high-resolution topography and DREEM images, we used highly doped silicon cantilevers (PPP-FMR from Nanosensor; 2.8 N/m) instead of metal coated cantilevers, because the radius of curvature of the metal coated tip is ~ 20 nm, while that for the non-coated tip is ~ 7 nm. The conductivity of the doped cantilevers is comparable to that of the metal coated tips. It should be noted, however, that these doped silicon tips are easily oxidized, which results in the formation of a nanometer thin non-conductive oxidized layer. Consequently, to make a conductive connection between the cantilever and the external input power source, it is essential to penetrate the oxide layer. As described below, we have devised a straightforward method for making a reliable connection, by scraping the cantilever chip and simultaneously coating it with colloidal liquid silver. The silver on the chip makes contact with the metallic tip holder for the Asylum AFM system. For use with instruments that do not have grounded tip holders, ground wires can be attached with patch of liquid silver.

Detailed instructions for cantilever preparation. A small amount of the colloidal liquid silver (Ted Pella Inc. product #16034) is spread on a clean glass slide. The cantilever is held with one pair of tweezers. Another pair of tweezers is dipped in the liquid silver, and these silver coated tweezers are used to scrape and coat the edges of the silicon chip and the silicon surface of the chip on the side opposite from the cantilever tip. The scraping removes the oxidized silicon (SiO_2) layer on the surface and replaces it with a conductive silver layer. This process simultaneously scratches away the oxide layer and covers the silicon with silver, preventing any oxidation and forming a conductive layer that can be easily connected to the external electrical sources. Once the coating is completed, the silver coated chip is allowed to dry for ~5 minutes, and it then can be loaded into the AFM.

Substrate grounding

In our setup, the bias is applied to the tip and the sample is grounded. To ground the sample, which is deposited on mica, we use liquid silver to connect a thin piece of mica to a glass slide, and we also make a connection to ground using liquid silver. Specifically, after the sample has been deposited on mica, a box cutter is used to cleave a thin layer of mica containing the deposited samples (on the topside). The opposite side of the mica (the downside), which does not contain the sample, is coated with liquid silver and held in the air until the liquid silver is dried. This sample is then attached to a glass slide with liquid silver.

To prepare the glass slide, the center of a glass slide is coated with a patch of liquid silver at least as large as the mica. A streak of silver leading from this central patch to one of the furthest sides is painted, and the streak is continued for a short distance on the other side of the glass slide to ensure that it makes proper contact with the metal on the AFM base for grounding. The silver-coated mica is placed, silver side down, on the wet silver patch, and the slide is allowed to dry for ~30 minutes. It is important not to press down too hard when placing the mica on the silver patch to avoid causing patches where there is no silver.

Selection of the imaging conditions

AFM topographic images are collected in standard repulsive intermittent contact mode at the fundamental resonance frequency (ω_1) (MFP-3D AFM, Asylum Research). With the cantilevers used in this study (PPP-FMR from Nanosensor; 2.8 N/m), we found that the highest quality topographic images were obtained with a vibration amplitude of 30 to 50 nm and a set point such that the force on the sample is minimized, while maintaining a repulsive interaction with surface. Not surprisingly, we found that the quality of the DREEM images is highly dependent on the quality of the topographic images. To determine the optimum AC and DC biases for DREEM imaging, we measured A_{ω_2} and collected images as a function of V_{AC} and V_{DC}

(from 0 to 20 V and -2.5 to 2.5 V, respectively) using the instrumental setup shown in Figure 1. Images were collected on two different custom modified MFP-3D Asylum Research AFMs in two different labs (DAE and HW).

The DREEM images of the nucleosomal arrays were taken at V_{AC} ~ 20 V and V_{DC} between ±2.5 V, depending on the tip. The magnitude of the applied DC voltage was adjusted based on the resolution and contrast of the DREEM images to achieve the highest signal to noise ratios. When the tip is in contact with mica in either repulsive or attractive mode and tuned near the optimum DC voltage, A_{ω_2} increases linearly upon varying V_{AC} from 0 to 20V, as expected (Mikamo-Satoh et al., 2009). The time constant for collection of the DREEM signal at ω_2 is 1 ms. Images were collected at a scan speed of 2 Hz, and the scan speed is limited by collection of the topographic signal, not the DREEM signal. The largest amplitudes that we employed for DREEM imaging at the first overtone are very small (~ 1 nm) compared to the mechanical vibration (30 to 50 nm) at the fundamental frequency, which prevents crosstalk of the electrical signal into the topographic signal. As expected, we also did not detect any crosstalk from the topography in the DREEM images (Figure S1), and no distinct signals are observed without applied biases. Also, we found that the larger protein-DNA complexes gave a better contrast between the DNA and the proteins, as compared to the smaller ones, probably because the greater amount of protein provides higher contrast. Similar to conventional AFM imaging techniques, DREEM imaging also can also experience tip artifacts, which are primarily due to the asymmetry in the electric field between the cantilever and sample surface. For example, in some cases, half-moon like asymmetries, with one side of the signal consistently higher than the other side, are seen in the same orientation for all complexes and proteins in a single image. Such images are discarded and not included in analyses. As with artifacts in conventional AFM images, these artifacts can be identified by their repetitive nature and by scanning at various angles, speeds, and size ranges, and by rotating the sample. Similar to conventional AFM

imaging, preparing clean samples and conductive tips, and driving the tip at the minimum possible drive amplitude minimize the artifacts.

Sample preparation, deposition and analysis

The $BaTiO_3$ (BTO) thin film was fabricated by atomic layer controlled growth with in-situ monitoring using high pressure reflection high energy electron diffraction (RHEED) (Choi et al., 2004; Eom et al., 1992). External electrical fields (DC bias) applied through a conductive AFM cantilever during scanning were used to locally polarize the BTO thin film and to generate a surface pattern with different polarization states.

Reconstitution of nucleosomes was done using a linear 2743 bp DNA substrate that was generated through XbaI restriction digestion of plasmid containing 601 (pGEM-3z/601, Addgene) nucleosomal positioning sequences (Lowary and Widom, 1998). The reconstitution was done using histones (EpiCypher) and the salt dialysis method (Carruthers et al., 1999). In some cases, the nucleosomes were crosslinked with gluteraldehyde (Sigma Aldrich) for 30 min at room temperature. The crosslinked or uncrosslinked nucleosomal arrays were deposited on the freshly prepared aminopropyl triethoxy silane (APTES)-treated mica surface and incubated for 10-15 minutes before rinsing (Shlyakhtenko et al., 2003). *Taq* MutS, human MutSα and MutLα were purified using the protocols published previously (Geng et al., 2012; Sass et al., 2010). For MutS-DNA complexes, the proteins and DNA were incubated together at room temperature for two minutes, crosslinked with 0.8% gluteraldehyde for 1 min. The DNA is a linearized 2030 base pair plasmid containing a single GT-mismatch (375 base pairs from one end) (Geng et al., 2012), which serves as a recognition site for MutS and hMutSα. Some protein-DNA complexes were purified using an approximately two-centimeter agarose bead gel filtration column prior to deposition to remove excess free proteins. The complexes were deposited on APTES-treated mica (Shlyakhtenko et al., 2003), immediately rinsed with water, and dried with

nitrogen, before imaging. The mica was exposed to APTES for only 15 minutes so that the mica surface contains a low density of amine groups. The DNA lengths were measured using the Asylum Research Software. The volume analysis was done as described previously (Ratcliff and Erie, 2001; Yang et al., 2003).

Supplemental References

Albrecht, T.R., Grütter, P., Horne, D., and Rugar, D. (1991). Frequency modulation detection using high-Q cantilevers for enhanced force microscope sensitivity. J. Appl. Phys. *69*, 668-673.

Carruthers, L.M., Tse, C., Walker, K.P., 3rd, and Hansen, J.C. (1999). Assembly of defined nucleosomal and chromatin arrays from pure components. Methods Enzymol. *304*, 19-35.

Choi, K.J., Biegalski, M., Li, Y.L., Sharan, A., Schubert, J., Uecker, R., Reiche, P., Chen, Y.B., Pan, X.Q., Gopalan, V.*, et al.* (2004). Enhancement of ferroelectricity in strained BaTiO3 thin films. Science *306*, 1005-1009.

Colchero, J., Gil, A., and Baró, A. (2001). Resolution enhancement and improved data interpretation in electrostatic force microscopy. Physical Review B *64*.

Ding, X.D., An, J., Xu, J.B., Li, C., and Zeng, R.Y. (2009). Improving lateral resolution of electrostatic force microscopy by multifrequency method under ambient conditions. Appl. Phys. Lett. *94*, 223109.

Eom, C.B., Cava, R.J., Fleming, R.M., Phillips, J.M., Vandover, R.B., Marshall, J.H., Hsu, J.W., Krajewski, J.J., and Peck, W.F., Jr. (1992). Single-Crystal Epitaxial Thin Films of the Isotropic Metallic Oxides Sr1-xCaxRuO3 (0 le x le 1). Science *258*, 1766-1769.

García, R., and Perez, R. (2002). Dynamic atomic force microscopy methods. Surf. Sci. Rep.

Geng, H., Sakato, M., DeRocco, V., Yamane, K., Du, C., Erie, D.A., Hingorani, M., and Hsieh, P. (2012). Biochemical analysis of the human mismatch repair proteins hMutSalpha MSH2(G674A)-MSH6 and MSH2-MSH6(T1219D). The Journal of biological chemistry *287*, 9777-9791.

Giessibl, F.J. (1995). Atomic resolution of the silicon (111)-(7x7) surface by atomic force microscopy. Science *267*, 68-71.

Gil, A., Colchero, J., Gómez-Herrero, J., and Baró, A. (2003). Electrostatic force gradient signal: resolution enhancement in electrostatic force microscopy and improved Kelvin probe microscopy. Nanotechnology *14*, 332.

Glatzel, T. (2003). Amplitude or frequency modulation-detection in Kelvin probe force microscopy. Appl. Surf. Sci. *210*, 84-89.

Hong, J., Kahng, D., Shin, J., Kim, H., and Khim, Z. (1998). Detection and control of ferroelectric domains by an electrostatic force microscope. Journal of Vacuum Science & Technology B: Microelectronics and Nanometer Structures *16*, 2942.

Hong, J., Park, S., and Khim, Z. (1999). Measurement of hardness, surface potential, and charge distribution with dynamic contact mode electrostatic force microscope. Rev. Sci. Instrum. *70*, 1735.

Hoummady, M., and Farnault, E. (1998). Enhanced sensitivity to force gradients by using higher flexural modes of the atomic force microscope cantilever. Applied Physics A: Materials Science & Processing *66*, 361-364.

Leung, C., Kinns, H., Hoogenboom, B.W., Howorka, S., and Mesquida, P. (2009). Imaging surface charges of individual biomolecules. Nano Lett. *9*, 2769-2773.

Leung, C., Maradan, D., Kramer, A., Howorka, S., Mesquida, P., and Hoogenboom, B.W. (2010). Improved Kelvin probe force microscopy for imaging individual DNA molecules on insulating surfaces. Appl. Phys. Lett. *97*, 203703.

Lowary, P.T., and Widom, J. (1998). New DNA sequence rules for high affinity binding to histone octamer and sequence-directed nucleosome positioning. J. Mol. Biol. *276*, 19-42.

Martin, Y., Williams, C.C., and Wickramasinghe, H.K. (1987). Atomic force microscope–force mapping and profiling on a sub 100-Å scale. J. Appl. Phys. *61*, 4723-4729.

Mikamo-Satoh, E., Yamada, F., Takagi, A., Matsumoto, T., and Kawai, T. (2009). Electrostatic force microscopy: imaging DNA and protein polarizations one by one. Nanotechnology *20*, 145102.

Nonnenmacher, M., O'Boyle, M.P., and Wickramasinghe, H.K. (1991). Kelvin probe force microscopy. Appl. Phys. Lett. *58*, 2921.

Rast, S., Wattinger, C., Gysin, U., and Meyer, E. (2000). The noise of cantilevers. Nanotechnology *11*, 169.

Ratcliff, G.C., and Erie, D.A. (2001). A novel single-molecule study to determine protein--protein association constants. JACS *123*, 5632-5635.

Sass, L.E., Lanyi, C., Weninger, K., and Erie, D.A. (2010). Single-molecule FRET TACKLE reveals highly dynamic mismatched DNA-MutS complexes. Biochemistry *49*, 3174-3190.

Shlyakhtenko, L.S., Gall, A.A., Filonov, A., Cerovac, Z., Lushnikov, A., and Lyubchenko, Y.L. (2003). Silatrane-based surface chemistry for immobilization of DNA, protein-DNA complexes and other biological materials. Ultramicroscopy *97*, 279-287.

Takagi, A., Yamada, F., Matsumoto, T., and Kawai, T. (2009). Electrostatic force spectroscopy on insulating surfaces: the effect of capacitive interaction. Nanotechnology *20*, 365501.

Tevaarwerk, E., Keppel, D.G., Rugheimer, P., Lagally, M.G., and Eriksson, M.A. (2005). Quantitative analysis of electric force microscopy: The role of sample geometry. Rev. Sci. Instrum. *76*, 053707.

Yang, Y., Wang, H., and Erie, D.A. (2003). Quantitative characterization of biomolecular assemblies and interactions using atomic force microscopy. Methods *29*, 175-187.